


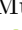
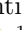
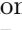
















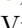
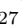
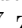
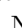






New Methods for Offline GstLAL Analyses

Prathamesh Joshi ^{1,2,3,*} Leo Tsukada ^{1,2,4,5,†} Chad Hanna^{1,2,6,7} Shomik Adhicary ^{1,2} Debnandini Mukherjee ^{8,9} Wanting Niu ^{1,2} Shio Sakon ^{1,2} Divya Singh ^{1,2,10} Pratyusava Baral ¹¹ Amanda Baylor ¹¹ Kipp Cannon ¹² Sarah Caudill^{13,14} Bryce Cousins ^{15,1,2} Jolien D. E. Creighton ¹¹ Becca Ewing^{1,2} Heather Fong^{16,12,17} Richard N. George ¹⁸ Patrick Godwin ^{19,1,2} Reiko Harada^{12,17} Yun-Jing Huang ^{1,2} Rachael Huxford²⁰ James Kennington ^{1,2} Soichiro Kuwahara^{12,17} Alvin K. Y. Li ^{12,17} Ryan Magee ²¹ Duncan Meacher ¹¹ Cody Messick ¹¹ Soichiro Morisaki ²² Alexander Pace ^{1,2} Cort Posnansky ^{1,2} Anarya Ray ^{11,23} Surabhi Sachdev ^{3,11} Stefano Schmidt ^{24,25} Urja Shah ³ Ron Tapia^{1,7} Koh Ueno ¹² Aaron Viets ²⁶ Leslie Wade²⁷ Madeline Wade ²⁷ Zach Yarbrough ²⁸ and Noah Zhang ³

¹*Department of Physics, The Pennsylvania State University, University Park, PA 16802, USA*

²*Institute for Gravitation and the Cosmos, The Pennsylvania State University, University Park, PA 16802, USA*

³*School of Physics, Georgia Institute of Technology, Atlanta, GA 30332, USA*

⁴*Department of Physics and Astronomy, University of Nevada,
Las Vegas, 4505 South Maryland Parkway, Las Vegas, NV 89154, USA*

⁵*Nevada Center for Astrophysics, University of Nevada, Las Vegas, NV 89154, USA*

⁶*Department of Astronomy and Astrophysics, The Pennsylvania State University, University Park, PA 16802, USA*

⁷*Institute for Computational and Data Sciences, The Pennsylvania State University, University Park, PA 16802, USA*

⁸*NASA Marshall Space Flight Center, Huntsville, AL 35811, USA*

⁹*Center for Space Plasma and Aeronomic Research,
University of Alabama in Huntsville, Huntsville, AL 35899, USA*

¹⁰*Department of Physics, University of California, Berkeley, CA 94720, USA*

¹¹*Leonard E. Parker Center for Gravitation, Cosmology, and Astrophysics,
University of Wisconsin-Milwaukee, Milwaukee, WI 53201, USA*

¹²*RESCEU, The University of Tokyo, Tokyo, 113-0033, Japan*

¹³*Department of Physics, University of Massachusetts, Dartmouth, MA 02747, USA*

¹⁴*Center for Scientific Computing and Data Science Research,
University of Massachusetts, Dartmouth, MA 02747, USA*

¹⁵*Department of Physics, University of Illinois, Urbana, IL 61801 USA*

¹⁶*Department of Physics and Astronomy, University of British Columbia, Vancouver, BC, V6T 1Z4, Canada*

¹⁷*Graduate School of Science, The University of Tokyo, Tokyo 113-0033, Japan*

¹⁸*Center for Gravitational Physics, University of Texas at Austin, Austin, TX 78712, USA*

¹⁹*LIGO Laboratory, California Institute of Technology, MS 100-36, Pasadena, California 91125, USA*

²⁰*Minnesota Supercomputing Institute, University of Minnesota, Minneapolis, MN 55455, USA*

²¹*LIGO Laboratory, California Institute of Technology, Pasadena, CA 91125, USA*

²²*Institute for Cosmic Ray Research, The University of Tokyo,
5-1-5 Kashiwanoha, Kashiwa, Chiba 277-8582, Japan*

²³*Center for Interdisciplinary Exploration and Research in Astrophysics, Northwestern University, IL 60201, USA*

²⁴*Nikhef, Science Park 105, 1098 XG, Amsterdam, The Netherlands*

²⁵*Institute for Gravitational and Subatomic Physics (GRASP),
Utrecht University, Princetonplein 1, 3584 CC Utrecht, The Netherlands*

²⁶*Concordia University Wisconsin, Mequon, WI 53097, USA*

²⁷*Department of Physics, Hayes Hall, Kenyon College, Gambier, Ohio 43022, USA*

²⁸*Department of Physics and Astronomy, Louisiana State University, Baton Rouge, LA 70803, USA*

(Dated: August 4, 2025)

In this work, we present new methods implemented in the GstLAL offline gravitational wave search. These include a technique to reuse the matched filtering data products from a GstLAL on-line analysis, which hugely reduces the time and computational resources required to obtain offline results; a technique to combine these results with a separate search for heavier black hole mergers, enabling detections from a larger set of gravitational wave sources; changes to the likelihood ratio which increases the sensitivity of the analysis; and two separate changes to the background estimation, allowing more precise significance estimation of gravitational wave candidates. Some of these methods increase the sensitivity of the analysis, whereas others correct previous mis-estimations of sensitivity by eliminating false positives. These methods have been adopted for GstLAL's offline results during the fourth observing run of LIGO, Virgo, and KAGRA (O4). To test these new methods, we perform an offline analysis over one chunk of O3 data, lasting from May 12 19:36:42 UTC 2019 to May 21 14:45:08 UTC 2019, and compare it with previous GstLAL results over the same period of time. We show that cumulatively these methods afford around a 50% - 100% increase in sensitivity in the highest mass space, while simultaneously increasing the reliability of results, and making them more reusable and computationally cheaper.

I. INTRODUCTION

By detecting gravitational waves (GWs) from the merger of compact objects like black holes and neutron stars, the LIGO Scientific, Virgo and KAGRA Collaborations (LVK) have revolutionized the field of gravitational wave astronomy. GW150914 was the first such detection of a GW [1], and since then close to 250 GWs have been detected [2]. While individual detections can often yield important scientific results, e.g., GW150914 [3], GW170817 [4, 5], GW200105 and GW200115 [6], even richer scientific implication can be extracted from a collection of GW detections. To this end, the LVK maintains a *catalog* of transient GW detections, called the Gravitational Wave Transient Catalog (GWTC). To date, four versions of the catalog have been released: GWTC-1 [7], GWTC-2 [8], GWTC-2.1 [9], and GWTC-3 [10]. These help inform results related to testing the theory of general relativity [11–14], cosmology [15, 16], black hole properties and formation mechanisms [17–19], and binary population and merger rates [20–22].

These results are enabled by GW search pipelines, by detecting GWs in the data produced by GW detectors, such as the two LIGO detectors [23], the Virgo detector [24], and the KAGRA detector [25]. The contents of the catalog are usually compiled from rigorous high-latency “offline” GW searches rather than low-latency “online” ones. GstLAL [26–29] is one such GW search pipeline. Like other modeled GW searches, it makes use of a bank of waveform templates predicted by general relativity. These templates are cross-correlated against the data in a process called matched filtering to calculate the signal-to-noise ratio (SNR). GstLAL performs matched filtering in the time domain [26, 27, 30]. This process is used to identify periods of time possibly containing GW signals, which are called “triggers”. Matched filtering is also used to inform the background data, against which triggers are ranked to evaluate their significance. A likelihood ratio (LR) [31, 32] is calculated as the ranking statistic. Triggers with a high LR are called GW candidates. The LRs of candidates are then compared with the LR statistics of background triggers, and using the livetime of the analysis, a false alarm rate (FAR) is calculated for every candidate. Some of these techniques are used by other GW search pipelines, such as IAS [33, 34], MBTA [35, 36], PyCBC [37–39], and SPIIR [40, 41].

This paper is structured as follows. In Sec. II, we describe the GstLAL offline workflow. Sec. III is dedicated to describing the new features introduced in the GstLAL offline workflow in the lead up to, and during the fourth observing run (O4) of the LVK. Sec. IV contains the results of the tests performed to evaluate these features, and to compare them against third observing run (O3) results.

II. OVERVIEW OF THE GSTLAL OFFLINE ANALYSIS

The GstLAL offline analysis can be broadly divided into two stages, each of which is further divided into smaller stages. These are:

1. setup stage
 - (a) template bank creation stage
 - (b) power spectral density (PSD) measurement stage
 - (c) singular value decomposition (SVD) of templates and template whitening stage
2. data processing stage
 - (a) matched filtering stage
 - (b) rank stage

A. Template bank creation stage

For O4, two GstLAL template banks, namely the stellar-mass black hole and intermediate-mass black hole (IMBH) banks were generated using *manifold* [42, 43], which is a binary-tree approach to template bank generation. All templates in both banks neglect eccentricity, higher-order modes, precession and matter effects. They additionally assume that the spins of each component object are aligned with an orbital angular momentum of the binary. This is done to limit the dimensionality of the bank, and hence the number of templates contained in it. While both of these banks are used to implement all-sky searches, in this work we will refer to the former search as the “AllSky search”, while the latter will continue to be called the IMBH search.

1. AllSky template bank

The AllSky template bank includes templates in the binary neutron star (BNS), neutron star–black hole binary (NSBH), and binary black hole (BBH) parameter spaces [44], consisting of 1815963 templates in total. This bank is used for the GstLAL online analysis, as well as for the bulk of the GstLAL offline results. It extends from component masses of $1 M_{\odot}$ to $200 M_{\odot}$. The absolute values of dimensionless spin components are capped at 0.99 for components of the binary template that are black holes (defined as having a mass above $3M_{\odot}$), and 0.05 for components that are neutron stars (defined as having a mass below $3M_{\odot}$). Specifications of the AllSky template bank are shown in Tab. I, and Fig. 1 shows a representation of the AllSky bank in the m_1 - m_2 space. Readers are referred to Ref. [45] for more details about the AllSky template bank.

* prathamesh.joshi@ligo.org

† leo.tsukada@ligo.org

Parameter	AllSky Template Bank
Primary mass, m_1	$\in [1.0, 200M_\odot]$
Secondary Mass, m_2	$\in [1.0, 200M_\odot]$
Mass ratio, $q = m_1/m_2$	$\in [1, 20]$
Total mass, $m_1 + m_2$	$\in [2.0, 400M_\odot]$
Dimensionless spin, $s_{i,z}$, for $m_i \leq 3.0M_\odot$	$ s_{i,z} \leq 0.05$
Dimensionless spin, $s_{i,z}$, for $m_i \geq 3.0M_\odot$	$ s_{i,z} \leq 0.99$
Lower frequency cut-off	15 Hz ^a
Higher frequency cut-off	1024 Hz
Waveform approximant	IMRPhenomD
Minimum match	97 %
PSD	O4 projected PSD ^b
Total number of templates	1815963

^a Due to enforcement of a maximum duration of 128 seconds, some lower mass templates have a higher lower frequency cut-off

^b [46]

TABLE I. Parameters of the GstLAL O4 AllSky template bank.

In comparison, the GstLAL O3 AllSky template bank covered component masses $m_i \in [1.0, 400]M_\odot$. It also limited templates to spin-aligned systems and set an upper limit of 0.05 on the magnitude of the spin for component masses below $3M_\odot$. The spin magnitudes for component masses above $3M_\odot$ were set to 0.999. The O3 template bank used a minimum match value of 99% for the BNS space, in contrast to the O4 value of 97%. The parameter choices of the O3 template bank is shown in Table II of Ref. [8]. As a result of different template bank generation algorithms and parameter choices, the O3 AllSky bank consisted of 1758763 templates.

The upper mass limit of the O4 AllSky bank is lower as compared to that of the O3 one. This was intentionally done, with the O4 IMBH bank (explained below) covering this space instead. The other differences in the O4 AllSky bank as compared to the O3 one were motivated by better template coverage of parameter spaces of interest with the new manifold method, while still minimizing the number of templates required.

2. IMBH template bank

In contrast to the AllSky bank, the IMBH bank is much smaller, and is only used to augment the GstLAL offline results in the IMBH parameter space. The IMBH bank covers the mass parameter space higher than what the AllSky template bank targets, as shown in Table II. The lower limit of m_1 is set to $203 M_\odot$ such that the IMBH bank is an extension to the AllSky bank and the templates of the two template banks do not overlap in the m_1 - m_2 space, as shown in Fig. 1. The dimensionless spins extend from -0.69 to 0.99. The reason for the lower cutoff (-0.69) to be higher than that of the AllSky bank (-0.99) is to prevent the ringdown frequency of the templates from getting close to the lower frequency cutoff for matched filtering used by the IMBH search (10 Hz).

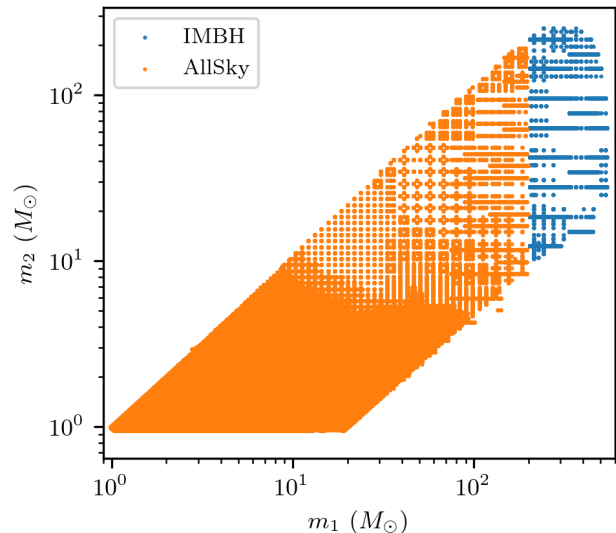


FIG. 1. AllSky templates and IMBH templates on the $\log(m_1)$ - $\log(m_2)$ plane. Here, the orange dots with $m_1 \leq 200M_\odot$ are AllSky templates and blue dots with $m_1 \geq 200M_\odot$ are IMBH templates.

Parameter	IMBH Template Bank
Primary mass, m_1	$\in [203, 543M_\odot]$
Secondary Mass, m_2	$\in [10, 255M_\odot]$
Mass ratio, $q = m_1/m_2$	$\in [1, 20]$
Total mass, $m_1 + m_2$	$\in [215, 660M_\odot]$
Dimensionless spin, $s_{i,z}$	$s_{i,z} \in [-0.69, 0.99]$
Lower frequency cut-off	10 Hz
Higher frequency cut-off	1024 Hz
Waveform approximant	IMRPhenomD
Minimum match	99 %
PSD	O4 projected PSD ^a
Total number of templates	14728

^a [46]

TABLE II. Parameters of the GstLAL O4 IMBH template bank.

Details of the parameters of the IMBH bank are shown in Tab. II. Fig. 1 also shows a plot of the IMBH bank in the m_1 - m_2 space.

3. Population model

Population models provide weights to templates which represent our prior knowledge of the astrophysical distribution of GW sources [47]. This is used in the likelihood ratio (LR) calculation, as well as to compute probabilities of astrophysical origin of candidates [48]. In O4, the population models for both the AllSky and IMBH banks were generated using manifold. They implement a Salpeter

mass function to assign weights to templates, defined as:

$$p(m_1, m_2, s_{1,z}, s_{2,z}) \propto \frac{m_1^{-2.35}}{m_1 - m_{\min}} \quad (1)$$

For both the AllSky and IMBH population models, the value of m_{\min} is set to 0.8, which is slightly less than the minimum mass in the combined AllSky+IMBH template bank. The Salpeter function was chosen as a simple equation that works well over a large range of masses to approximate the astrophysical distribution of GW sources inferred by previous studies [20–22].

B. PSD measurement stage

The PSD is the frequency representation of detector noise, and is used in the matched filter calculation. This is done by whitening both the data and the templates with the PSD measured from the data. GstLAL has the ability to measure the PSD of the data in real time and dynamically whiten the data during the matched filtering stage. However, this ability does not extend to template whitening, and the templates need to be whitened before the analysis starts. The PSD used for this purpose is measured from the data in the PSD measurement stage. The data is first divided into smaller pieces of up to 8 hours depending on the continuity of segments when each detector is operational. The PSD over each such piece of data is individually measured, and the median over each frequency bin is taken, which removes any transient noise features contributing to the PSD of a single piece of data. The resultant PSD is used to whiten the templates. More details about PSD measurement can be found in Ref. [26].

C. SVD of templates and template whitening stage

Next, as discussed in Ref. [45], the template bank is sorted by linear combinations of their Post-Newtonian phase coefficients [49] and split into “template bins”, each of around 1000 templates, which are whitened using the median PSD described above. These template bins further go through a process called SVD to save computational cost of the matched filtering [50]. The templates in one such template bin are processed together for the purpose of matched filtering and background estimation, constituting a single matched-filtering job, and hence this template binning allows for a large-scale parallelization in both online and offline workflows.

D. Matched filtering stage

Each template within a template bin is matched filtered with the data, producing triggers. Alongside SNR, a signal consistency statistic, called ξ^2 is also calculated for every trigger [26]. Triggers with contribution from

only one detector (referred to as a “single detector trigger”), during a time when multiple detectors were operational (referred to as “coincident time”), are considered to originate from noise [51]. This is because GW signals are expected to be correlated across detectors, unlike noise. The SNR and ξ^2 statistics of noise triggers are added to the template bin’s common noise background, which is later one of the inputs used to calculate the LR for triggers.

In parallel, the GW candidates are extracted from the triggers. This is done by retaining only those triggers within a template bin that have the highest SNR in a 0.2 second window. A single GW signal can create triggers via multiple templates, and with current detector sensitivities, it is highly unlikely for multiple GW signals to occur in the same 0.2 second window [citeRelton2021]. Hence, with this “clustering” over SNR, duplicate triggers from a single common signal are removed, reducing the amount of data downstream stages need to process. The processes of populating the background and generating candidates are done in parallel for every template bin.

E. Rank stage

In this stage, the significance of candidates is evaluated, and the results of the search are produced. First, the LR is calculated for every candidate forwarded by the matched filtering stage. One of the ingredients in calculating the LR is the SNR- ξ^2 background populated by the matched filtering stage. To model a smooth distribution of SNR- ξ^2 statistics, a kernel density estimate (KDE) is applied to the background, and the resulting probability density is used for LR evaluation. This gives us the probability that the (SNR, ξ^2) of a given candidate arises from noise. This is one of the many terms in the LR equation. More details on the LR calculation can be found in Ref. [32].

Next, the candidate list is pruned again by performing a second round of clustering. This time, it is performed *across* template bins. The candidate with the highest LR in an 8 second window is retained. Apart from eliminating candidates originating from noise, this ensures that a single GW signal will have at most one candidate originating from it in the entire analysis.

Finally, to convert the LR to a FAR, we need the LR distribution of noise triggers from every template bin [31, 52]. If we use the same set of noise triggers as was used to populate the SNR- ξ^2 background, the LR distribution will not be well defined at higher LRs due to lower number of statistics. Additionally, since these noise triggers were obtained during the livetime of the analysis, the lowest FAR would be bound by 1 per livetime. To solve this problem, GstLAL extrapolates the set of noise triggers from every template bin by drawing samples of SNR and ξ^2 , and assigning random templates as well as arrival times and phases. This is a computation-

ally cheap operation, and under the assumption that the template, time and phase distribution of noise triggers is uniform, this process can effectively extrapolate the LR distribution of noise triggers to high LRs, enabling the FAR calculation of even the most significant candidates.

However, this process does not work particularly well for low LRs. To fix this, we can make one more assumption, that at low LRs, even the candidates originate from noise. Consequently, the low LR distribution of candidates is the same as the low LR distribution of noise triggers, and the former can be used to inform the latter. The method of doing so is called the “extinction model”. Once the LR distribution of noise triggers is calculated, it can be combined with the livetime of the analysis to produce a FAR for every candidate.

III. NEW METHODS

A. Online Rank

During every observing run, the full data are analyzed in near-real time by the GstLAL low-latency or “online” analysis. The various stages of the online analysis, up to the matched filtering stage, are largely similar to those of the offline analysis. Consequently, during O4, a new method has been adopted to outsource the GstLAL offline analysis’ matched filtering stage to the GstLAL online analysis. This method is called an “online rank”. A description of the differences between the GstLAL online and offline analyses, as well as a detailed description of the online rank method is provided in Ref. [53].

As described in Ref. [53], the online rank method significantly reduces the computational cost and time needed for offline results. Matched filtering is the vast majority of the computational burden of a modeled GW search. By eliminating the need to repeat matched filtering a second time for the offline analysis, this method affords a 50% reduction in computational cost over the course of an observing run, and specifically a 95 - 99.8% reduction in time required to obtain offline results.

B. Dropped Data Refiltering

In order to make the online rank results even more reliable and sensitive, we can augment the inputs to the online rank with triggers and background data from times that the online analysis dropped. To do this, for every job in the online analysis, we take the list of time periods when each job was functional and producing output. We then subtract that from the list of times a traditional offline analysis would have analyzed, which is calculated by external tools as an extra step in the setup stage of the offline workflow. This leaves us with a list of times that a particular job has dropped. We calculate such a “dropped data segments” for every job. Then, we can set up a traditional offline analysis using these dropped

data segments. The only unusual aspect of this procedure is that while setting up this “dropped data refiltering” analysis, each job has its own segments list rather than a global one for every job. An example of such a list of dropped data segments is shown in Fig. 2

By combining the online rank inputs with the results of the dropped data refiltering analysis, we can be sure the online rank produces offline results for exactly the same periods of time that the traditional offline analysis would have. The typical amount of dropped data for any job is around 5% of the total time covered by the offline segments [53].

A point to note is that while we can add data to the online rank using this method, and we also have the ability to remove data to the granularity of the snapshots recorded by the online analysis (4 hours, see Ref. [53]), we cannot remove arbitrarily small amounts of data from an online rank. This means that we cannot incorporate more refined data quality information, such as small vetoed periods of time that only become available after the online analysis has finished.

C. IMBH Analysis

The AllSky template bank was designed to be a general-purpose bank for an online analysis. To obtain more comprehensive offline results, we want to augment the results of the AllSky search with a search for IMBH mergers. The GstLAL O4 offline results are obtained by performing a search over the data using the IMBH template bank described in Sec. II, which is then combined with the AllSky search into a single set of results using the procedure described in the following subsection.

As shown in Ref. [29, 32], the LR contains a term to test the consistency of signals across the network of detectors, for observed parameters like SNR and the coalescence time and phase. These parameters can only take on certain possible physical values for a network of detectors and follow specific correlations that indicate whether a GW trigger is of astrophysical origin. The correlation among these observables and their joint distribution depend on trigger’s template, and hence in principle this signal consistency test should be modified for every template. However, for the purpose of pre-computation efficiency, we adopt a BNS template with component masses of $1.4 M_{\odot}$, which is shown to be effective *throughout* Allsky template bank. In contrast, the mass range of the IMBH template bank is so high that this empirical fact might not be true, and hence for the IMBH analysis we use a template with component masses of $60 M_{\odot}$.

Other differences in search settings between the AllSky and the IMBH searches include different lower frequency cutoffs during matched filtering. AllSky uses 15 Hz, but the IMBH search uses 10 Hz as these binaries merge at lower frequencies. The Allsky search uses the TaylorF2 [55] approximant upto a chirp mass of 1.73 for cost effectivity and the SEOBNRv4_ROM [56] beyond that,

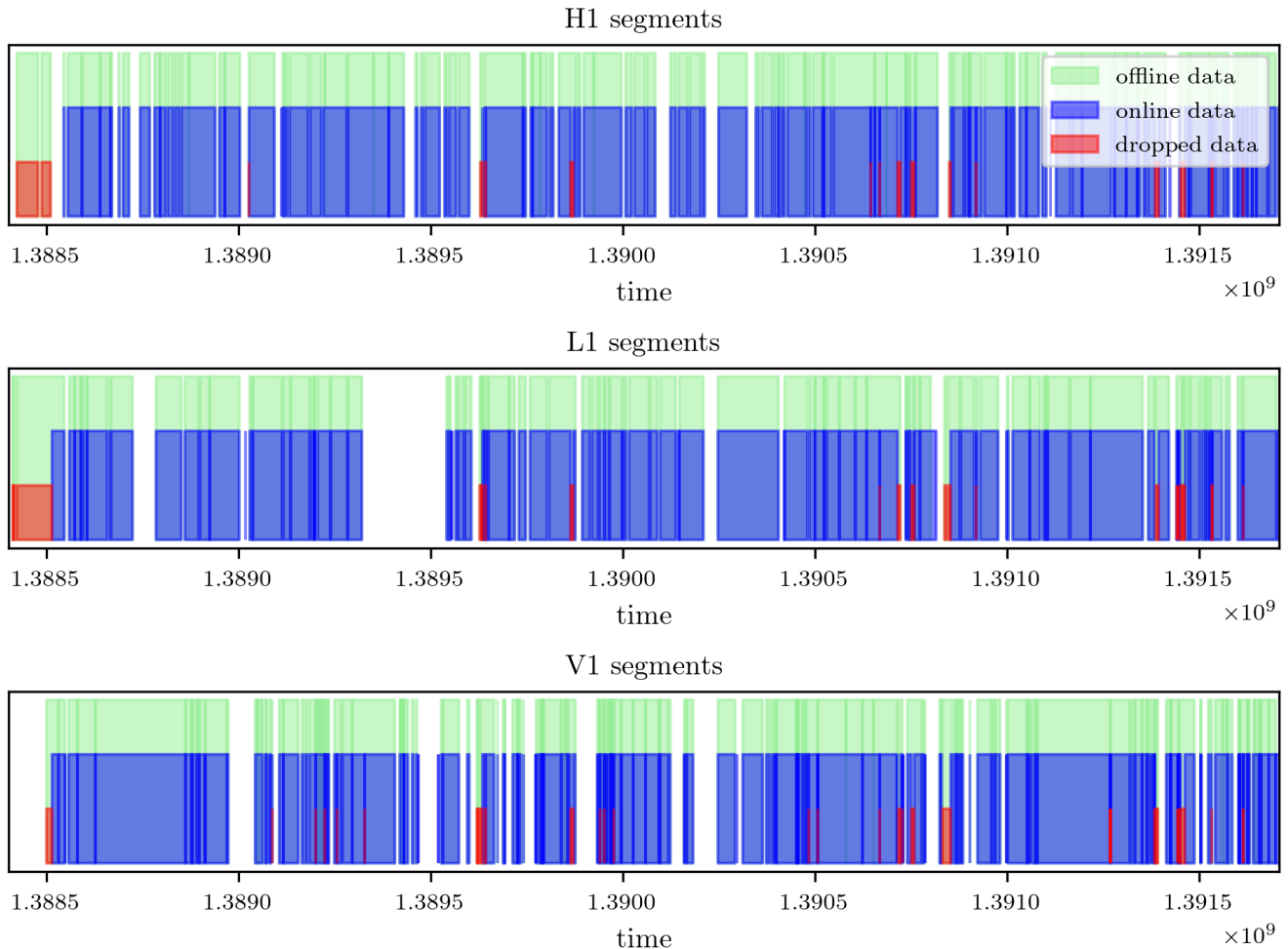


FIG. 2. An example of a particular online job's list of dropped data segments. The dropped data segments at the very start of the plot are because of slightly different start times of the online and offline analysis, whereas the ones after that are because of online analysis having failed to analyze those times, either because the data for those times was dropped in order to keep up with incoming live data, or because the online job was not functioning at that time. We see that the amount of dropped data is not too large, but the segments are dispersed throughout the period of the analysis. Ref. [53] shows that a typical online analysis drops around 5% of the total data. This data can be filtered offline in order to augment the online rank's results. This particular plot was made using a GstLAL online analysis that participated in the mock data challenge [54].

while the IMBH search only uses the SEOBNRv4_ROM as an approximant. Note that template placement for both banks was done with the IMRPhenomD approximant [57], but we do not expect this inconsistency to be problematic. Similarly, the autocorrelation length used by the Allsky search for calculating the ξ signal-based veto [26] is 701 sample points upto a chirp mass of 1.73, and 351 above that. The IMBH search uses a value of 351 sample points throughout, due to a shorter duration of the waveforms. For this reason, the minimum number of samples included in a given time slice [26] is 512 for IMBH and 2048 for Allsky. For similar reasons, while splitting the IMBH bank into template bins, the templates are sorted by their duration which is found to be more effective for this part of the parameter space, rather than

sorting by linear combinations of their Post-Newtonian phase coefficients.

It is known that the candidates in the IMBH search are overwhelmingly single-detector candidates. This was true even for triggers, before any clustering was done. For example, in the test described in Sec. IV, out of the total candidates reported by the IMBH search, 92.75% were found to be single-detector candidates, and out of the set of triggers, 98.57% were single-detector triggers. The corresponding numbers for the Allsky search are 3.37% and 35.07% respectively. While the root cause of this is not well understood, the vastly different percentages of single-detector triggers in the Allsky and IMBH searches indicate that this arises from the matched filtering and coincidence formation of IMBH templates, rather than

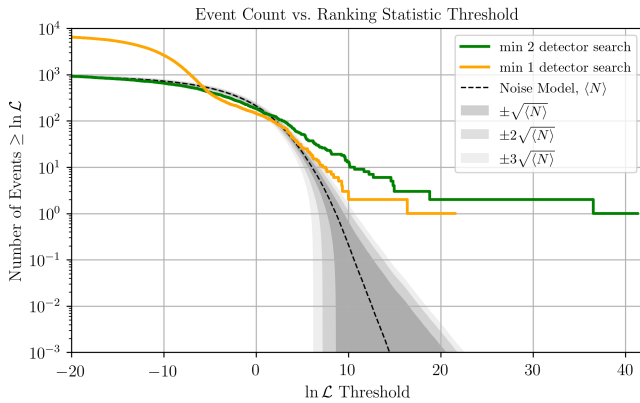


FIG. 3. This plot shows the results of two IMBH searches: one which only considers triggers with two or more detectors contributing to it, and another with no such restriction. The plot also shows the noise LR statistics of the former search for reference. We can see that the LR statistics of the candidates of the search that only processes triggers with two or more detectors is well behaved, whereas the other one is not. This is because the IMBH search, if allowed to process single-detector triggers recovers an overwhelming amount of them, and the LRs (and hence FARs) of single-detector triggers are difficult to accurately calculate. As a result, for O4, GstLAL’s IMBH search doesn’t process single-detector triggers.

anything to do with the LR.

The LRs of single-detector candidates are notoriously difficult to estimate [58], and so is the process of LR extrapolation of noise triggers. Consequently, the FARs of single-detector candidates are less reliable than those of multi-detector candidates, and a search with such a high percentage of single-detector candidates is unlikely to be functional. As a result, for GstLAL’s O4 offline results, the IMBH search ignores single detector triggers, and only processes those with multiple contributing detectors. The effects on the LR statistics of candidates if single-detector triggers are allowed to be processed are shown in Fig. 3.

D. Combining the AllSky and IMBH analyses

In order to combine Allsky and IMBH searches into a single search, one can naively treat every template bin from both the AllSky and IMBH searches as though they are part of a bigger AllSky+IMBH joint template bank. This means after each template bin assigns LRs to its candidates, these candidates would be clustered together based on their LR, and the noise LR statistics of each template bin will be combined via the extinction model. An implicit assumption of this method is that each template bin’s candidate and noise LR statistics in the noise regime are approximately the same. However, with the different parameter space and settings of the IMBH search as compared to AllSky, this assumption is no longer valid, and hence the naively combined results

can be severely biased. To this end, we have developed a new scheme to combine the AllSky and IMBH analyses into a single search.

We first calculate a *weight* for each individual analysis, based on each analysis’ contribution to the final clustered set of candidates. This was done using injection campaigns for both analyses. Injections are simulated GW signals inserted into the data. This weight represents the number of GW signals we expect each analysis to contribute independent of the other, and is a combination of the analysis’ sensitivity, and the expected number of GW signals in each parameter space. The weights for the AllSky and IMBH analyses were found to be 0.94 and 0.06. This result was also verified by summing over the population model weights for the AllSky and IMBH templates after taking into consideration the different SNR detection thresholds of the two analyses.

Next, the FARs of each analysis’ candidates are scaled up by the inverse of their respective weights. Note that FARs are assigned to each analysis separately, and hence the FARs of candidates in the noise regime in both analyses are guaranteed to be distributed similarly as they only depend on the livetime of the search. Since the weights sum up to 1, this new set of candidates is guaranteed to have a consistent distribution of FARs in the noise regime, i.e., there will be on average livetime (expressed in hours) number of candidates with a FAR of one per hour or lower, and so on. Candidates from both analyses are then clustered together by retaining the lowest FAR candidate in an 8 second window. The LRs of the candidates are then re-calculated based on their new FARs, using the inverse of the mapping used by the AllSky analysis to convert LRs into FARs. In principle, any such mapping would have worked, and the AllSky mapping is chosen only for convenience.

E. Modularity and reusability of results

A general theme of the development work prior to and during O4 has been about reducing the duplication of computations done elsewhere. Apart from the online rank described in Sec. III A, we have made the GstLAL offline workflow more modular and flexible. In general, offline analyses over large periods of data (such as GstLAL’s offline results for O4) are performed in small chunks, each of around 1 week of data. Alongside the ability to extract any amount of matched filtering data from the online analysis as specified by the user (to the granularity of 4 hours) [53], the GstLAL offline workflow also has the ability to use the data from any set of offline chunks specified by the user. Consequently, one can specify any period of data covered by any combination of online and offline analyses using any template banks, and they can be combined into a single result. Therefore, once a period of data has been matched filtered by a particular template bank via either an online (complemented by the dropped data refiltering) or offline analysis, it never

needs to be filtered using that template bank again. This has greatly reduced the computational and time burden of GstLAL operations as well as development work during O4.

F. Ranking statistic improvements

GstLAL has adopted the likelihood ratio as the ranking statistic to evaluate the statistical significance of GW candidates [31, 32]. The likelihood ratio in GstLAL takes the form of

$$\mathcal{L} = \frac{P(\vec{O}, \vec{\rho}, \xi^2, \vec{t}, \vec{\phi}, \theta | \mathcal{H}_s)}{P(\vec{O}, \vec{\rho}, \xi^2, \vec{t}, \vec{\phi}, \theta | \mathcal{H}_n)}, \quad (2)$$

which represents the probability of obtaining a set of observable parameters, e.g., SNR for each detector $\vec{\rho}$, under the signal hypothesis (\mathcal{H}_s) relative to that under the noise hypothesis (\mathcal{H}_n). Here, ρ refers to the SNR of a single detector, and we will use this terminology for the rest of this subsection to maintain compatibility with others papers on this subject. The improvements in this ranking statistic prior to O4's start are thoroughly described in Ref. [32], which include the upgraded $\rho - \xi^2$ signal model and removal of signal contamination. In particular, the upgraded $\rho - \xi^2$ signal model achieved $\sim 20\%$ increase in the search sensitivity, and hence has led to a major contribution of GstLAL to LVK's GW detections in O4 so far.

Apart from the improvements mentioned above, we have modified the $\rho - \xi^2$ noise model to make more accurate estimate of event's significance in some part of (ρ, ξ^2) parameter space. As described in Ref. [32, 51], GstLAL collects single-detector triggers during coincident time into the 2D $\rho - \xi^2$ histogram and estimates its noise model. Since templates of lighter binary systems such as BNS tend to not couple with non-Gaussian noise, e.g., *glitches*, most of noise triggers associated with such low-mass templates are expected to be modeled by the Gaussian noise component. For each detector, trigger's SNR is calculated as square root of a quadrature sum of SNR values given by two orthogonal templates through matched-filtering, each of which follows the normal distribution. Therefore, the SNR-squared follows a chi-square distribution with two degree-of-freedom regardless of the observed ξ^2 value.

Also, according to the formalism of the upgraded $\rho - \xi^2$ signal model described in Ref. [32], the expected value of ξ^2 in the *noise* model can be also given by substituting the mismatch factor $k = 1$, i.e., maximum mismatch between a hypothetical signal and template, into Eq.(40) of Ref. [32],

$$\langle \xi^2 \rangle = \frac{1}{N} \left\{ N + (\rho^2 - 1) \vec{R}^\dagger \vec{R} \right\} \sim 1, \quad (3)$$

where N is a auto-correlation length used for ξ^2 calculation and \vec{R} is an auto-correlation function of a given

template normalized so that $R[0] = 1$. This approximation holds because an auto-correlation of compact binary coalescence (CBC) signals in general sharply peaks at the center where two templates exactly align, and hence $\vec{R}^\dagger \vec{R} \ll N(R[0])^2 = N$. Therefore, triggers from the Gaussian noise component are distributed near $\xi^2 = 1$ and decaying toward higher SNR. Consistently, this behavior is illustrated in Fig. 4, which shows a $\rho - \xi^2$ noise model for one of the low-mass template bins collected for LIGO Hanford detector during the mock data campaign described in Ref. [54] with the lightblue dashed line as a $\xi^2 = 1$ contour. In contrast, a tail of the distribution, which extends toward higher SNR and ξ^2 , is known as non-Gaussian noise component.

However, during the online analysis of O4, we discovered that the Gaussian component of the noise model deviates from the expected chi-square distribution significantly at $\rho > 9$ because very few or zero noise trigger populates such a higher SNR regime and the KDE applied as a smoothing process does not complement the lack of triggers sufficiently. See Fig. 5 where a 2D $\rho - \xi^2$ noise model is sliced at the $\xi^2 = 1$ contour and projected onto the ρ dimension. Note that the expected chi-squared distribution shown as a black curve is given by

$$p(\rho) = \chi_2^2(\rho) \frac{d\rho^2}{d\rho} \propto 2\rho e^{-\rho^2/2}. \quad (4)$$

Although, this disagreement can eventually improve if we keep the analysis running and collect noise triggers long enough, early phase of the online analysis is likely to overestimate an event's significance due to this bias and send out a public alert, e.g., S240422ed [59][60]. Also, we cannot guarantee that this bias does not exist even in an offline analysis where noise triggers collected entirely from single (or subset of) observing run are considered. Therefore, the objective here is to modify the tail of the Gaussian noise component such that it can produce more accurate noise model even with fewer collected triggers and eventually prevent a potential false claim of GW detections.

To this end, after collecting enough noise triggers, we extrapolate the trigger counts along a given iso- ξ^2 contour using the bulk of the Gaussian component so that its tail part follows the expected distribution shown in Eq. (4). This process is iterated over a range of $-0.5 < \log \xi^2 < 0.5$ and finally the KDE is applied to produce a smoother distribution. The green curve in Fig. 5 shows that the noise model after this extrapolation closely follows the expected distribution in black curve. Although it can be slightly above the black curve, one can see that it still provides much more accurate estimate of the event's significance than the red curve without the extrapolation at $\rho > 9$.

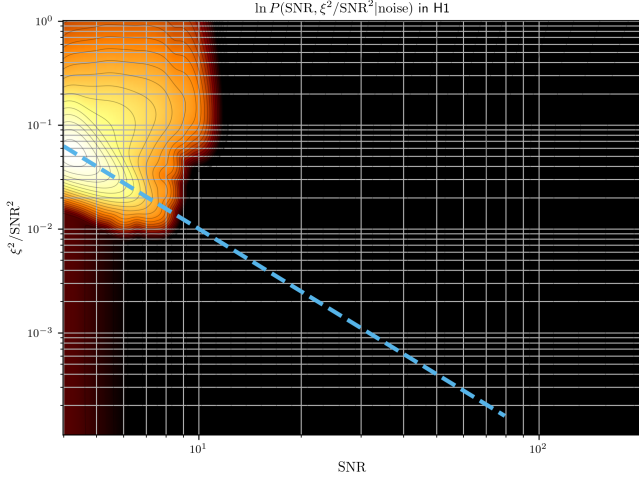


FIG. 4. Example of ρ - ξ^2 noise model for one of the low-mass template groups collected for LIGO Hanford detector during the mock data campaign described in [54] with the lightblue dashed line as a $\xi^2 = 1$ contour

G. New Extinction Model

A set of candidates undergo two rounds of clustering, the first with other candidates within the template bin, and the second with candidates from all template bins. These clustering processes alter the LR distribution of candidates. Consequently, the LR distribution of the noise triggers which gets used to convert the LR of candidates to FARs also needs to undergo these clustering processes. The new extinction model quantifies the change in LR distribution due to clustering, and applies it to the LR distribution on noise triggers. To mimic clustering, this is performed in two steps, the first within the noise triggers of a template bin, and the second with noise triggers across template bins. Additionally, the new extinction model enforces that any template bin's contribution to the noise LR distribution is proportional to its contribution to the LR distribution of candidates. Both of these features ensure that the FARs assigned to candidates are more accurate than the old method, i.e., stitching the LR distribution of candidates below some LR threshold to the LR distribution of noise triggers [61].

Let $y(L)$ be the histogram of noise triggers that GstLAL stores in order to estimate the complementary cumulative distribution function of noise LRs, $N(L)$. The two are related in the following way:

$$N(L) = A \int_L^\infty y(L^*) dL^* \quad (5)$$

$$N_c(L) = A \int_L^\infty y_c(L^*) dL^* \quad (6)$$

where A is some normalization constant, and the subscript c denotes the clustered version of the respective

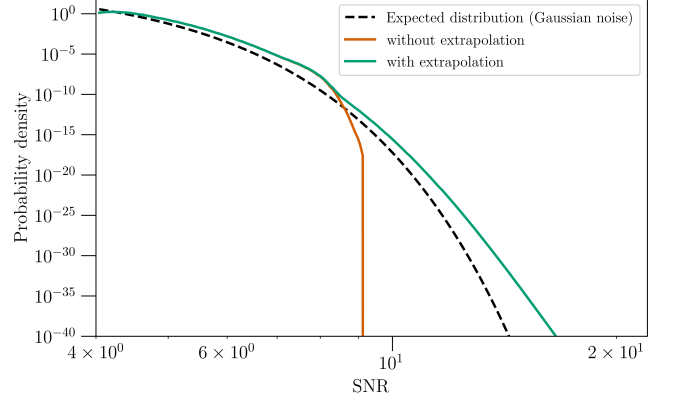


FIG. 5. 2D ρ - ξ^2 noise model sliced at the $\xi^2 = 1$ contour and projected onto the ρ dimension. The noise model with the extrapolation closely follows the expected distribution in black curve at $\rho > 9$ as opposed to the red curve without the extrapolation.

functions. Equivalently,

$$y(L) = -\frac{dN(L)}{dL} \quad (7)$$

The new extinction model assumes that the process of obtaining triggers above a certain LR threshold L^* in the clustering interval is a Poisson process, with Poisson rate given by:

$$\lambda = c \times N(L^*) \quad (8)$$

where c is another normalization constant. Hence the probability that some trigger with $LR = L^*$ survives clustering, i.e. that there are no triggers with a higher LR than L^* in the clustering interval is the Poisson probability for zero events.

$$P_{\text{survival}}(L^*) = e^{-\lambda} = e^{-cN(L^*)} \quad (9)$$

Hence, we can add the effect of clustering to $y(L)$, by multiplying it with the survival probability.

$$y_c(L) = y(L)e^{-cN(L)} \quad (10)$$

Substituting Eq. (10) in Eq. (6), it follows

$$\begin{aligned} N_c(L) &= A \int_L^\infty y(L^*) e^{-cN(L^*)} dL^* \\ &= - \int_{N(L)}^{N(\infty)} e^{-cN(L^*)} dN(L^*) \\ &= \frac{1}{c} [1 - e^{-cN(L)}] \end{aligned} \quad (11)$$

where $N(\infty) = 0$. Since GstLAL deals with the complementary cumulative histogram of LRs, $n(L)$, rather than probability density, we can convert this to the histogram

form by adding another normalization constant. After absorbing relevant constants in A and c , we get:

$$n_c(L) = A[1 - e^{-cn(L)}] \quad (12)$$

In order to find the constants A and c , the new extinction model performs a curve fit of $n_c(L)$ to the LR histogram of candidates. This is first done within a template bin, and after all of those clustered bin-specific noise histograms are added together, it is performed across template bins. The constant A takes care of the relative contributions of template bins to the candidate set, whereas the constant c takes care of the effect of clustering on the set of candidates. The curve fitting is performed from the 50th percentile to the 99th percentile of the complementary cumulative histogram of candidate LRs. This is empirically known to be a region of well-modeled noise candidates. The uncertainties in the curve fitting can be calculated from the assumption that a particular realization of the value of $y(L)$ is Poisson distributed. Hence,

$$\sigma_{y(L)} = \sqrt{y(L)} \quad (13)$$

$$\begin{aligned} \sigma_{N(L)}^2 &= \int_{L^*}^{\infty} \sigma_{y(L^*)}^2 dL^* \\ &= \int_{L^*}^{\infty} y(L^*) dL^* \\ \sigma_{N(L)} &= \sqrt{N(L)} \end{aligned} \quad (14)$$

The effect of applying the new extinction model on the noise triggers is shown in Fig. 6. We can see that in the noise regime (i.e. 50th percentile to the 99th percentile), the noise LR histogram with the new extinction model is very close to the candidate histogram. This shows that the new extinction model is successful in applying the effects of candidate clustering and relative contributions of template bins to the candidate set. By adopting the new extinction model, we get more accurate FARs, since the noise LR distribution used to assign FARs is more accurate than the old method. The new extinction model has also been adopted for GstLAL’s online operations in the second part of the fourth observing run (O4b).

IV. RESULTS

A. Data set

To test the new methods described in Sec. III, and to serve as a trial run for GstLAL’s O4 offline results, we set up a GstLAL analysis over 1 chunk of LIGO and Virgo O3 data. The data extends for approximately one week, from May 12 19:36:42 UTC 2019 to May 21 14:45:08 UTC 2019. Since Ref. [53] already tests the online rank feature and concludes it is equivalent to a traditional offline analysis, we do not test that feature here, and directly set up an offline analysis over the data instead of running an online analysis and setting up an online rank based

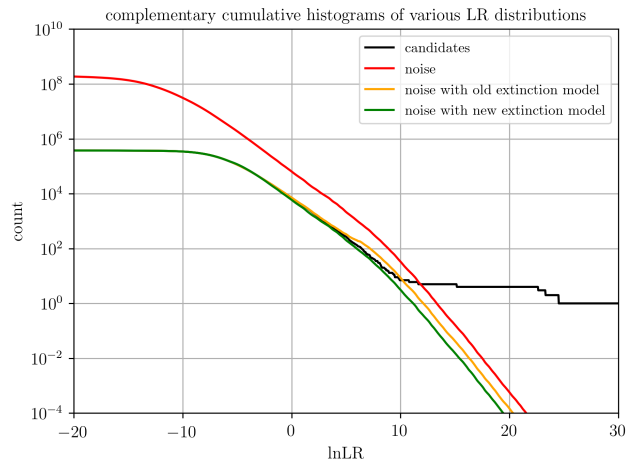


FIG. 6. Effect of applying the new extinction model on the noise LR histogram. The effects of candidate clustering and differing relative contributions of template bins to the candidate set are modeled by modifying the noise LR histogram, $n(L)$ to $A[1 - e^{-cn(L)}]$. The values of A and c are found by curve fitting the modified noise LR histogram to the candidate LR histogram. We can see that this process is effective from the fact that the noise LR histogram with the new extinction model is very close to the candidate LR histogram in the noise region (low LR).

on that. The offline analysis included a search with the AllSky bank, and a search with the IMBH bank, which were then combined into a single search using the procedure described in Sec. III, referred to as the “O4 analysis” hereafter. It also includes the LR improvements, the extrapolation in $\rho - \xi^2$ noise model and new extinction model. We then compared the results to GstLAL’s O3 offline results over the same period of data, referred to as the “O3 analysis” hereafter. Also, note that the O3 analysis uses the O3 template bank described in Sec. II A 1. Both analyses also included the same injection campaign. The details of the distribution of injections in this campaign can be found in Ref. [8, 62].

B. Candidate lists

This set of data contains 6 GW candidates previously reported in Ref. [8, 9]. Both the O4 and O3 analyses recover all 6 candidates in the list of top 10 candidates, as summarized in Tab. III and Tab. IV respectively. The O4 search recovers all 6 confidently with a FAR below 1/month, whereas the O3 search only recovers 5 of the 6 confidently.

C. Sensitivity comparison

To compare the sensitivities of the O4 and O3 analyses, we use the sensitive volume-time, or VT of the

Rank	FAR (Hz)	SNR	UTC Time	Found Detectors	Operating Detectors	m_1 (M_\odot)	m_2 (M_\odot)	s_{1z}	s_{2z}
1	2.69×10^{-38}	24.51	2019-05-21 07:43:59	H1,L1	H1,L1	54.75	29.25	-0.2011	-0.2011
2	1.46×10^{-20}	13.35	2019-05-19 15:35:44	H1,L1	H1,L1	83.15	79.75	0.6033	0.6033
3	8.60×10^{-19}	14.14	2019-05-21 03:02:29	H1,L1	H1,L1,V1	213.1	137.4	0.8712	0.8712
4	3.72×10^{-16}	12.30	2019-05-13 20:54:28	H1,L1,V1	H1,L1,V1	50.36	48.29	0.6033	0.6033
5	3.56×10^{-12}	10.48	2019-05-17 05:51:01	H1,L1	H1,L1,V1	50.36	40.86	0.7889	0.7889
6	1.65×10^{-10}	10.88	2019-05-20 10:35:19	L1,V1	H1,L1,V1	442.1	218.2	0.8646	0.8646
7	9.71×10^{-9}	8.41	2019-05-14 06:54:16	H1,L1	H1,L1	54.75	57.08	-0.2320	-0.2320
8	1.25×10^{-8}	13.00	2019-05-15 06:27:00	H1,L1	H1,L1	543.3	63.58	0.2638	0.2638
9	1.46×10^{-8}	13.67	2019-05-14 04:01:29	H1,L1	H1,L1	414.9	144.7	0.8778	0.8778
10	1.88×10^{-8}	8.39	2019-05-18 20:43:46	L1,V1	H1,L1,V1	414.9	218.2	0.8646	0.8646

TABLE III. The candidate list for the offline search using GstLAL's O4 methods. The search is run over a week of O3 data. The first, second, third, fourth, fifth, and seventh candidates in this list correspond to the GWs GW190521_074359, GW190519_153544, GW190521_030229, GW190513_205428, GW190517_055101, and GW190514_065416, previously reported in Ref. [8, 9]. The remaining 4 candidates all arise from the IMBH search, and have not been previously reported. Given the uncertainty surrounding the IMBH space of GW signals, we make no claims regarding the origin of these 4 candidates

Rank	FAR (Hz)	SNR	UTC Time	Found Detectors	Operating Detectors	m_1 (M_\odot)	m_2 (M_\odot)	s_{1z}	s_{2z}
1	1.04×10^{-43}	24.43	2019-05-21 07:43:59	H1,L1	H1,L1	56.33	37.81	-0.0015	0.4993
2	4.33×10^{-21}	11.68	2019-05-13 20:54:28	H1,L1	H1,L1	60.74	32.32	0.8530	-0.1904
3	1.58×10^{-18}	13.03	2019-05-19 15:35:44	H1,L1	H1,L1	103.40	11.61	0.0925	-0.9660
4	2.35×10^{-11}	10.36	2019-05-17 05:51:01	H1,L1,V1	H1,L1,V1	49.39	39.63	0.6712	0.8675
5	2.80×10^{-10}	12.94	2019-05-21 03:02:29	H1,L1,V1	H1,L1,V1	139.70	2.92	-0.2471	-0.0434
6	3.23×10^{-9}	8.42	2019-05-14 23:48:57	L1,V1	L1,V1	2.34	1.24	-0.0130	0.0336
7	3.16×10^{-7}	8.93	2019-05-20 06:39:01	H1,L1	H1,L1	4.94	1.10	0.3486	-0.0499
8	2.70×10^{-6}	8.33	2019-05-14 06:54:16	H1,L1	H1,L1	53.48	53.48	-0.5578	-0.5578
9	3.02×10^{-6}	9.63	2019-05-20 20:45:36	H1,V1	H1,L1,V1	21.42	18.44	0.6018	0.4931
10	3.85×10^{-6}	8.92	2019-05-17 14:43:16	H1,L1	H1,L1	19.96	1.24	-0.9457	0.0449

TABLE IV. The candidate list for the offline search using GstLAL's O3 methods. The search is run over a week of O3 data. The first, second, third, fourth, fifth, and eighth candidates in this list correspond to the GWs GW190521_074359, GW190513_205428, GW190519_153544, GW190517_055101, GW190521_030229, and GW190514_065416, previously reported in Ref. [8, 9].

two analyses as a metric. It represents the volume of 4-dimensional space-time where the search can typically identify GW signals. Since the times analyzed by both the O4 and O3 analyses is exactly the same, the VT s of the two analyses are a measure of their relative sensitivities. Furthermore, the VT s can be calculated for different mass ranges in order to estimate the relative sensitivities to different source classes. A plot of the ratio of the VT of the O4 analysis with and without the extrapolation in $\rho - \xi^2$ noise model, with the O3 analysis is shown in Fig. 7.

D. Performance of individual features

1. IMBH analysis

Here, we assess how much sensitivity we gain by combining the IMBH search with the AllSky search, compared to just the sensitivity of the AllSky search. The VT ratio of the O4 combined AllSky+IMBH search to that of the VT of the O4 AllSky search is shown in Fig. 8.

In addition to the 6% - 7% sensitivity improvement in the IMBH space as shown in Fig. 8, by adding the IMBH search to the AllSky one, the combined analysis becomes sensitive to a new parameter space, and has the ability to recover GW signals arising from intermediate-mass black hole mergers, which the AllSky search did not have by itself. This source class is particularly interesting and by detecting GWs from such mergers, we enable new scientific results [63].

2. Extrapolation in $\rho - \xi^2$ noise model

As mentioned previously, the extrapolation in $\rho - \xi^2$ noise model removes false positives in GW candidates. This implies that real GW signals can also be down-ranked accordingly and not be recovered as significantly as it would be without the extrapolation. To this end, we compare the VT s between with and without the extrapolation to assess the signal recovery performance. Fig. 9 shows the VT of the O4 analysis with the noise model extrapolation as a function of the recovered FAR for each category of injections, being relative to that for without

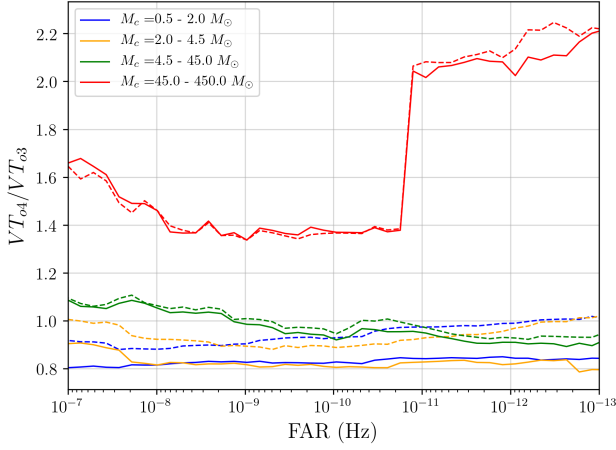


FIG. 7. VT ratios of the O4 search with the O3 search. The solid lines represent the full O4 search as compared to the O3 search, whereas the dashed lines represent the O4 search without the extrapolation in $\rho - \xi^2$ noise model as compared to the O3 search. Since the extrapolation removes false positives from the candidates, it corrects previous mis-estimations of the VT done in the O3 search, superficially lowering the O4 VT . The VT ratios of the two lowest mass bins are slightly less than 1. This is because the O3 template bank sampled the lower mass parameter space with a higher minimum match (0.99) as compared to O4 (0.97). Additionally, we see that the highest mass bin has a 50% - 100% increase in sensitivity, arising from the LR improvements and the additional IMBH search done in O4.

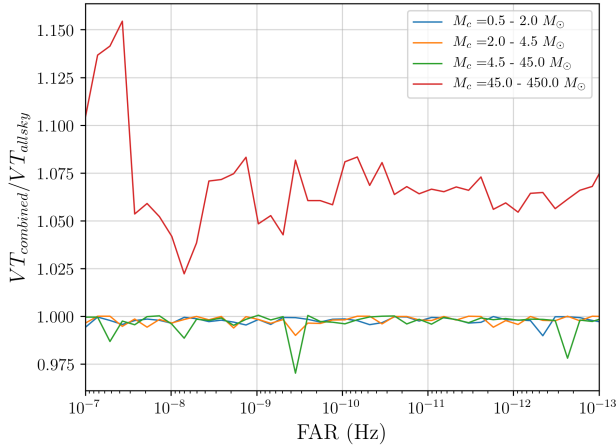


FIG. 8. This plot shows the ratio of VT of the O4 combined AllSky+IMBH search to that of the O4 AllSky search, and it shows us how much sensitivity we gain by combining the IMBH and AllSky searches, as compared to just the AllSky search. As expected the sensitivities of the 3 lowest mass bins are unchanged, since the IMBH bank is not sensitive in that region. The VT of the IMBH bin increases by 6% - 7%.

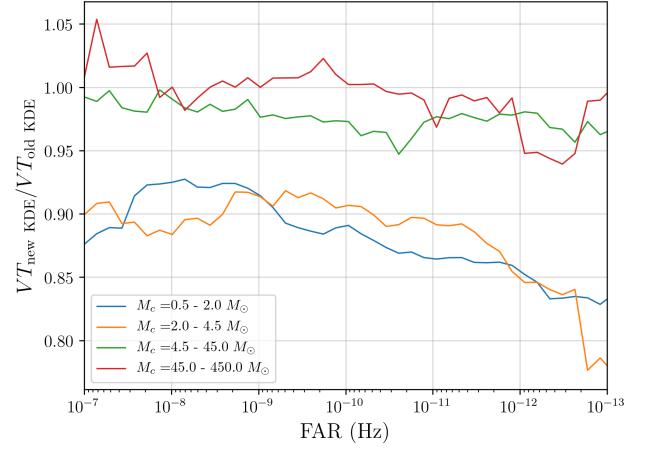


FIG. 9. VT ratio of the O4 search with the noise model extrapolation as compared to without. The extrapolation removes false positives from the set of candidates, and in the process also downweights a small amount of real GW signals. The former effect corrects the overestimate of VT that happens without the extrapolation, whereas the latter decreases the real sensitivity of the search. Both these effects contribute to the lower than 1 VT ratio seen here. This effect is mostly seen in the BNS and NSBH regions, whose VT goes down by 10% - 15%. The BBH and IMBH regions are mostly unaffected.

the extrapolation. Note that the sensitivity can decrease up to 15% for two lowest mass categories of the injections, e.g., blue and orange curves. This is because, as mentioned above, the noise model for lower mass templates tends to be dominated by the Gaussian component and hence the extrapolation is likely to be more impactful. In contrast, for heavier BBH templates, the non-Gaussian noise component overwhelms the Gaussian one and makes small changes at its tail part negligible. We also emphasize that this decrease in the search sensitivity does *not* necessarily indicate the lowered performance overall, but rather that the signal recovery without the extrapolation is overestimated and risks potential false positives.

3. Reliability of results

The new extinction model and LR improvements ensure the FARs of candidates are more accurate, and the extrapolation in $\rho - \xi^2$ noise model reduces the risk of false positives in the candidate set. All of these contribute to the O4 results being more reliable than before. This effect is difficult to measure since wrongly assigned FARs and false positives are rare. One possible metric is to see how many candidates in the injection campaign with a FAR below some threshold do not correspond to an injected GW signal. With a FAR threshold of one per day, this number for the O3 search is 53, represent-

ing 0.07% of all candidates. The corresponding number for the O4 search is 28, representing 0.03% of all candidates. For a higher FAR threshold of one per hour, the numbers for the O3 and O4 searches is 276 (0.35%) and 132 (0.15%). This shows that the new O4 methods are successful in lowering the number of false positives.

The O4 search includes the IMBH search. This parameter space is known to be particularly vulnerable to loud noise transients or non-gaussian transient “glitches” [64, 65]. If we only look at the O4 AllSky search, for a more direct comparison with O3, the numbers for the one-per-day and one-per-hour FAR thresholds are 23 (0.03%), and 110 (0.13%), showing an even higher efficacy of removing false positives.

V. CONCLUSION

In this work, we first gave an overview of the GstLAL offline analysis. This included descriptions of the GstLAL AllSky and IMBH template banks used in O4. We later described new methods in the GstLAL offline analysis introduced in the lead up to and during O4. These new methods are all used to obtain GstLAL’s offline results for O4.

The new methods include a way to outsource everything up to the matched filtering stage to an online analysis that had previously run on the same data. This, along with improvements to modularity of the workflow and reusability of results means that GW data only needs to be matched filtered with a given template bank only once during an observing run. The results of any such matched filtering, whether online or offline, and with any template bank can be combined into a single cohesive set of results.

The new methods also include a new IMBH offline search. This search only allows candidates with multiple contributing detectors, in order to make the search well-behaved and functional. A new method to combine the AllSky and IMBH searches was also introduced. It assigns a weight to each search by which the FARs of their candidates, calculated independently for each search, are scaled up. Afterwards, the set of candidates of the two searches can be combined in to single set of candidates.

Finally, we also discussed some changes to the LR calculation, introduced the extrapolation in $\rho - \xi^2$ noise model, as well as a new extinction model which enables a better estimation of the LR statistics of noise triggers.

To test these new methods, we set up an offline analysis over one week of O3 data, and compared the results with those obtained from the same data by GstLAL during O3. Both searches recovered the 6 previously reported GWs in the data in their list of top 10 candidates. The O4 search was able to do so confidently for all 6, whereas the O3 search managed it only for 5. We found that the sensitivity of the O4 search in the IMBH space increased by 50% - 100%. The VT in the BNS and NSBH space went down by 10% - 20% as a result of the extrapolation

in $\rho - \xi^2$ noise model, which reduces false positives and downweighting a small number of real GW signals accordingly. Without the new KDE, those VT s are very close to the O3 ones.

The new methods described in this work variously increase the sensitivity, reliability, or reusability of the GstLAL offline results. As a result, we expect GstLAL’s offline results to significantly contribute to the LVK’s scientific results in O4.

ACKNOWLEDGMENTS

This research has made use of data, software and/or web tools obtained from the Gravitational Wave Open Science Center (<https://www.gw-openscience.org/>), a service of LIGO Laboratory, the LIGO Scientific Collaboration (LSC) and the Virgo Collaboration. We especially made heavy use of the LVK Algorithm Library. LIGO was constructed by the California Institute of Technology and the Massachusetts Institute of Technology with funding from the United States National Science Foundation (NSF) and operates under cooperative agreements PHYS-0757058 and PHY-0823459. In addition, the Science and Technology Facilities Council (STFC) of the United Kingdom, the Max-Planck-Society (MPS), and the State of Niedersachsen/Germany supported the construction of Advanced Laser Interferometer Gravitational-Wave Observatory (aLIGO) and construction and operation of the GEO600 detector. Additional support for aLIGO was provided by the Australian Research Council. Virgo is funded, through the European Gravitational Observatory (EGO), by the French Centre National de Recherche Scientifique (CNRS), the Italian Istituto Nazionale di Fisica Nucleare (INFN) and the Dutch Nikhef, with contributions by institutions from Belgium, Germany, Greece, Hungary, Ireland, Japan, Monaco, Poland, Portugal, Spain.

The authors are grateful for computational resources provided by the LIGO Lab cluster at the LIGO Laboratory and supported by PHY-0757058 and PHY-0823459, the Pennsylvania State University’s Institute for Computational and Data Sciences gravitational-wave cluster, and supported by OAC-2103662, PHY-2308881, PHY-2011865, OAC-2201445, OAC-2018299, and PHY-2207728. The authors thank Thomas Dent (and the LVK CBC AllSky group) for sharing initial investigations on the Gaussian noise component of the $\rho - \xi^2$ noise model discussed in Sec. IIIF. The authors also thank Reed Essick (and the entire LVK Rates and Populations group) for developing the injection sets used in the calculation of the weights for the AllSky and IMBH analyses. LT acknowledges NASA 80NSSC23M0104 and the Nevada Center for Astrophysics for support. CH Acknowledges generous support from the Eberly College of Science, the Department of Physics, the Institute for Gravitation and the Cosmos, the Institute for Computational and Data Sciences, and the Freed Early Career Professorship. US

and SS acknowledge support from NSF PHY-2409714.

-
- [1] B. P. Abbott *et al.* (LIGO Scientific, Virgo), Phys. Rev. Lett. **116**, 061102 (2016), arXiv:1602.03837 [gr-qc].
- [2] L. Collaboration, “Ligo-virgo-kagra cumulative detection plot - o1-o4b,” (2024).
- [3] B. P. Abbott *et al.* (LIGO Scientific and Virgo Collaborations), Phys. Rev. Lett. **116**, 221101 (2016).
- [4] B. P. Abbott *et al.* (The LIGO Scientific Collaboration and the Virgo Collaboration), Phys. Rev. Lett. **121**, 161101 (2018).
- [5] B. P. Abbott *et al.* (LIGO Scientific Collaboration and Virgo Collaboration), Phys. Rev. Lett. **123**, 011102 (2019).
- [6] R. Abbott *et al.* (LIGO Scientific, KAGRA, VIRGO), Astrophys. J. Lett. **915**, L5 (2021), arXiv:2106.15163 [astro-ph.HE].
- [7] B. P. Abbott *et al.* (LIGO Scientific, Virgo), Phys. Rev. X **9**, 031040 (2019), arXiv:1811.12907 [astro-ph.HE].
- [8] Physical Review X **11**, 021053 (2021).
- [9] The LIGO Scientific Collaboration, The Virgo Collaboration, R. Abbott, *et al.*, “Gwtc-2.1: Deep extended catalog of compact binary coalescences observed by ligo and virgo during the first half of the third observing run,” (2021).
- [10] R. Abbott *et al.* (LIGO Scientific, VIRGO, KAGRA), “GWTC-3: Compact Binary Coalescences Observed by LIGO and Virgo During the Second Part of the Third Observing Run,” (2021), arXiv:2111.03606 [gr-qc].
- [11] B. P. Abbott *et al.* (The LIGO Scientific Collaboration and the Virgo Collaboration), Phys. Rev. D **100**, 104036 (2019).
- [12] S.-C. Yang, W.-B. Han, and G. Wang, Monthly Notices of the Royal Astronomical Society: Letters **499**, L53 (2020), https://academic.oup.com/mnrasl/article-pdf/499/1/L53/54638219/mnrasl_499_1_L53.pdf.
- [13] R. Abbott, H. Abe, F. Acernese, K. Ackley, N. Adhikari, R. Adhikari, V. Adkins, V. Adya, C. Affeldt, D. Agarwal, *et al.*, arXiv preprint arXiv:2112.06861 (2021).
- [14] J. M. Ezquiaga, Physics Letters B **822**, 136665 (2021).
- [15] D. C. H. J. . K. V. . R. D. . T. L. . . S. D. . V. S. . Y. S. . . 245 and L. C. O. C. A. I. . . H. G. . . H. D. A. . . M. C. . . P. D. . V. S. . 247, Nature **551**, 85 (2017).
- [16] T. L. S. Collaboration and the Virgo Collaboration, The Astrophysical Journal **909**, 218 (2021).
- [17] S. Wu, Z. Cao, and Z.-H. Zhu, Monthly Notices of the Royal Astronomical Society **495**, 466 (2020), <https://academic.oup.com/mnras/article-pdf/495/1/466/33387647/staa1176.pdf>.
- [18] H.-T. Wang, P.-C. Li, J.-L. Jiang, G.-W. Yuan, Y.-M. Hu, and Y.-Z. Fan, The European Physical Journal C **81**, 769 (2021).
- [19] Y. Bouffanais, M. Mapelli, F. Santoliquido, N. Giacobbo, U. N. Di Carlo, S. Rastello, M. C. Artale, and G. Iorio, Monthly Notices of the Royal Astronomical Society **507**, 5224 (2021), <https://academic.oup.com/mnras/article-pdf/507/4/5224/40392757/stab2438.pdf>.
- [20] T. L. S. Collaboration and the Virgo Collaboration, The Astrophysical Journal Letters **882**, L24 (2019).
- [21] T. L. S. Collaboration and the Virgo Collaboration, The Astrophysical Journal Letters **913**, L7 (2021).
- [22] R. Abbott *et al.* (KAGRA, VIRGO, LIGO Scientific), Phys. Rev. X **13**, 011048 (2023), arXiv:2111.03634 [astro-ph.HE].
- [23] J. Aasi *et al.* (LIGO Scientific), Class. Quant. Grav. **32**, 074001 (2015), arXiv:1411.4547 [gr-qc].
- [24] F. Acernese *et al.* (VIRGO), Class. Quant. Grav. **32**, 024001 (2015), arXiv:1408.3978 [gr-qc].
- [25] T. Akutsu *et al.*, Progress of Theoretical and Experimental Physics **2021** (2020), 10.1093/ptep/ptaa125, 05A101, <https://academic.oup.com/ptep/article-pdf/2021/5/05A101/37974994/ptaa125.pdf>.
- [26] C. Messick *et al.*, Phys. Rev. D **95**, 042001 (2017), arXiv:1604.04324 [astro-ph.IM].
- [27] S. Sachdev *et al.*, “The GstLAL Search Analysis Methods for Compact Binary Mergers in Advanced LIGO’s Second and Advanced Virgo’s First Observing Runs,” (2019), arXiv:1901.08580 [gr-qc].
- [28] K. Cannon *et al.*, “GstLAL: A software framework for gravitational wave discovery,” (2020), arXiv:2010.05082 [astro-ph.IM].
- [29] C. Hanna *et al.*, Phys. Rev. D **101**, 022003 (2020), arXiv:1901.02227 [gr-qc].
- [30] K. Cannon *et al.*, Astrophys. J. **748**, 136 (2012), arXiv:1107.2665 [astro-ph.IM].
- [31] K. Cannon, C. Hanna, and J. Peoples, “Likelihood-Ratio Ranking Statistic for Compact Binary Coalescence Candidates with Rate Estimation,” (2015), arXiv:1504.04632 [astro-ph.IM].
- [32] L. Tsukada, P. Joshi, S. Adhichary, R. George, A. Guimaraes, C. Hanna, R. Magee, A. Zimmerman, P. Baral, A. Baylor, K. Cannon, S. Caudill, B. Cousins, J. D. E. Creighton, B. Ewing, H. Fong, P. Godwin, R. Harada, Y.-J. Huang, R. Huxford, J. Kennington, S. Kuwahara, A. K. Y. Li, D. Meacher, C. Messick, S. Morisaki, D. Mukherjee, W. Niu, A. Pace, C. Posnansky, A. Ray, S. Sachdev, S. Sakon, D. Singh, R. Tapia, T. Tsutsui, K. Ueno, A. Viets, L. Wade, and M. Wade, (2023), arXiv:2305.06286 [astro-ph.IM].
- [33] T. Venumadhav, B. Zackay, J. Roulet, L. Dai, and M. Zaldarriaga, Phys. Rev. D **100**, 023011 (2019).
- [34] B. Zackay, L. Dai, T. Venumadhav, J. Roulet, and M. Zaldarriaga, Physical Review D **104** (2021), 10.1103/physrevd.104.063030.
- [35] F. Aubin, F. Brighenti, R. Chierici, D. Estevez, G. Greco, G. M. Guidi, V. Juste, F. Marion, B. Mours, E. Nitoglia, O. Sauter, and V. Sordini, Classical and Quantum Gravity **38**, 095004 (2021).
- [36] T. Adams, D. Buskulic, V. Germain, G. M. Guidi, F. Marion, M. Montani, B. Mours, F. Piergiovanni, and G. Wang, Classical and Quantum Gravity **33**, 175012 (2016).
- [37] T. D. Canton, A. H. Nitz, B. Gadre, G. S. C. Davies, V. Villa-Ortega, T. Dent, I. Harry, and L. Xiao, The Astrophysical Journal **923**, 254 (2021).
- [38] G. S. Davies, T. Dent, M. Tápai, I. Harry, C. McIsaac, and A. H. Nitz, Physical Review D **102** (2020), 10.1103/physrevd.102.022004.
- [39] A. H. Nitz, Physical Review D **98** (2018), 10.1103/PhysRevD.98.024050.
- [40] Q. Chu, Physical Review D **105** (2022), 10.1103/PhysRevD.105.024023.
- [41] Q. Chu, *Low-latency detection and localization of gravitational waves from compact binary coalescences*, Ph.D.

- thesis, The University of Western Australia (2017).
- [42] C. Hanna, J. Kennington, S. Sakon, S. Privitera, M. Fernandez, J. Wang, C. Messick, A. Pace, K. Cannon, P. Joshi, R. Huxford, S. Caudill, C. Chan, B. Cousins, J. D. E. Creighton, B. Ewing, H. Fong, P. Godwin, R. Magee, D. Meacher, S. Morisaki, D. Mukherjee, H. Ohta, S. Sachdev, D. Singh, R. Tapia, L. Tsukada, D. Tsuna, T. Tsutsui, K. Ueno, A. Viets, L. Wade, and M. Wade, *Phys. Rev. D* **108**, 042003 (2023).
 - [43] C. Hanna, “manifold,” <https://git.ligo.org/chad-hanna/manifold> (2024).
 - [44] B. Ewing, R. Huxford, D. Singh, L. Tsukada, C. Hanna, Y.-J. Huang, P. Joshi, A. K. Y. Li, R. Magee, C. Messick, A. Pace, A. Ray, S. Sachdev, S. Sakon, R. Tapia, S. Adhicary, P. Baral, A. Baylor, K. Cannon, S. Caudill, S. S. Chaudhary, M. W. Coughlin, B. Cousins, J. D. E. Creighton, R. Essick, H. Fong, R. N. George, P. Godwin, R. Harada, J. Kennington, S. Kuwahara, D. Meacher, S. Morisaki, D. Mukherjee, W. Niu, C. Posnansky, A. Toivonen, T. Tsutsui, K. Ueno, A. Viets, L. Wade, M. Wade, and G. Waratkar, (2023), [arXiv:2305.05625](https://arxiv.org/abs/2305.05625) [gr-qc].
 - [45] S. Sakon *et al.*, “Template bank for compact binary mergers in the fourth observing run of Advanced LIGO, Advanced Virgo, and KAGRA,” (2022), [arXiv:2211.16674](https://arxiv.org/abs/2211.16674) [gr-qc].
 - [46] “Ligo sensitivity (190 mpc) (used for o4 simulations),” (2022).
 - [47] H. K. Y. Fong, *From simulations to signals: Analyzing gravitational waves from compact binary coalescences*, Ph.D. thesis, Toronto U. (2018).
 - [48] A. Ray *et al.*, “When to Point Your Telescopes: Gravitational Wave Trigger Classification for Real-Time Multi-Messenger Followup Observations,” (2023), [arXiv:2306.07190](https://arxiv.org/abs/2306.07190) [gr-qc].
 - [49] S. Morisaki and V. Raymond, *Phys. Rev. D* **102**, 104020 (2020), [arXiv:2007.09108](https://arxiv.org/abs/2007.09108) [gr-qc].
 - [50] K. Cannon, A. Chapman, C. Hanna, D. Keppel, A. C. Searle, and A. J. Weinstein, *Phys. Rev. D* **82**, 044025 (2010).
 - [51] P. Joshi, L. Tsukada, and C. Hanna, “Background Filter: A method for removing signal contamination during significance estimation of a GstLAL analysis,” (2023), [arXiv:2305.18233](https://arxiv.org/abs/2305.18233) [gr-qc].
 - [52] K. Cannon, C. Hanna, and D. Keppel, *Phys. Rev. D* **88**, 024025 (2013), [arXiv:1209.0718](https://arxiv.org/abs/1209.0718) [gr-qc].
 - [53] P. Joshi, W. Niu, C. Hanna, R. Huxford, D. Singh, L. Tsukada, S. Adhicary, P. Baral, A. Baylor, K. Cannon, S. Caudill, M. W. Coughlin, B. Cousins, J. D. E. Creighton, B. Ewing, H. Fong, R. N. George, S. Ghosh, P. Godwin, R. Harada, Y.-J. Huang, C. Messick, S. Morisaki, D. Mukherjee, A. Pace, C. Posnansky, A. Ray, S. Sachdev, S. Sakon, U. Shah, R. Tapia, K. Ueno, A. Viets, L. Wade, M. Wade, Z. Yarbrough, and N. Zhang, “How many times should we matched filter gravitational wave data? a comparison of gstlal’s on-line and offline performance,” (2025), [arXiv:2505.23959](https://arxiv.org/abs/2505.23959) [gr-qc].
 - [54] S. S. Chaudhary *et al.*, “Low-latency alert products and their performance in anticipation of the fourth ligo-virgo-kagra observing run,” (in prep) (2023).
 - [55] A. Buonanno, B. R. Iyer, E. Ochsner, Y. Pan, and B. S. Sathyaprakash, *Phys. Rev. D* **80**, 084043 (2009).
 - [56] A. Bohé, L. Shao, A. Taracchini, A. Buonanno, S. Babak, I. W. Harry, I. Hinder, S. Ossokine, M. Pürrer, V. Raymond, T. Chu, H. Fong, P. Kumar, H. P. Pfeiffer, M. Boyle, D. A. Hemberger, L. E. Kidder, G. Lovelace, M. A. Scheel, and B. Szilágyi, *Phys. Rev. D* **95**, 044028 (2017).
 - [57] S. Khan, S. Husa, M. Hannam, F. Ohme, M. Pürrer, X. J. Forteza, and A. Bohé, *Phys. Rev. D* **93**, 044007 (2016).
 - [58] T. Callister, J. Kanner, T. Massinger, S. Dhurandhar, and A. Weinstein, *Classical and Quantum Gravity* **34**, 155007 (2017).
 - [59] Ligo Scientific Collaboration, VIRGO Collaboration, and Kagra Collaboration, *General Coordinates Network* **36236**, 1 (2024).
 - [60] The statistical significance of this candidate was subsequently estimated to be lower after collecting more noise triggers and the update alert was sent [66].
 - [61] C. Messick, *Detecting Gravitational Waves for Multi-Messenger Astro*, Ph.D. thesis (2019).
 - [62] L. S. Collaboration and V. Collaboration, “Gwtc-2 data release: Sensitivity of matched filter searches to binary black hole merger populations,” <https://dcc.ligo.org/P2000217/public>.
 - [63] R. Abbott, T. D. Abbott, F. Acernese, K. Ackley, C. Adams, N. Adhikari, R. X. Adhikari, V. B. Adya, C. Affeldt, D. Agarwal, *et al.*, *Astronomy & astrophysics* **659**, A84 (2022).
 - [64] S. Ghosh, K. Chandra, and A. Pai, *Physical Review D* **109** (2024), [10.1103/physrevd.109.064015](https://arxiv.org/abs/10.1103/physrevd.109.064015).
 - [65] R. Macas, J. Pooley, L. K. Nuttall, D. Davis, M. J. Dyer, Y. Lecoeuche, J. D. Lyman, J. McIver, and K. Rink, *Phys. Rev. D* **105**, 103021 (2022).
 - [66] Ligo Scientific Collaboration, VIRGO Collaboration, and Kagra Collaboration, *General Coordinates Network* **36812**, 1 (2024).